

CABLE NOISE IN IMPEDANCE MEASUREMENTS

BY

SCOTT A. DENENBERG

THESIS

Submitted in partial fulfillment of the requirements
for the degree of Master of Science in Electrical and Computer Engineering
in the Graduate College of the
University of Illinois at Urbana-Champaign, 2010

Urbana, Illinois

Adviser:

Professor Andreas Cangellaris

ABSTRACT

This thesis focuses on the analysis of cable noise in impedance measurements. Specifically, the focus is on cables being developed for embedded sensing applications. In many applications, such as torque sensing and embedded fatigue and corrosion sensing, it is not feasible to have the probe electronics unit in close proximity to the material under test (MUT). Therefore, a cabling system is necessary to connect the sensors located on the MUT to the probe electronics. In many of these applications, especially those which require a higher frequency range into the MHz, the cable system is a significant source of noise. Noise contributed by this section of the cabling system is especially detrimental because it is added prior to the probe electronics signal amplification and conditioning. This thesis describes a study of the electromagnetic attributes of the current prototype cabling design with particular emphasis on the quantitative investigation of its sources of noise. A method for quantifying measurement noise due to the presence of external electromagnetic radiation is presented, and it is shown that, in general, the prototype cabling has sufficient shielding. Furthermore, a model is presented that explains measurement variation due to cable shape changes, especially cable twisting.

To my family, for their love and support.

To JENTEK and my coworkers for their assistance and patience.

ACKNOWLEDGMENTS

I would like to thank Dr. Andreas Cangellaris for his encouragement, guidance and technical direction during the thesis process. Grateful acknowledgment is made to JENTEK Sensors and Dr. Neil Goldfine for technical guidance and financial support during the author's graduate studies. Thanks also to the many members of the JENTEK team who helped answer questions, gather information and take measurements during this project.

TABLE OF CONTENTS

CHAPTER 1	INTRODUCTION	1
1.1	Background	1
1.2	MWM Measurement Method	1
1.3	Prototype Cabling	4
CHAPTER 2	CABLE SHIELDING AND EXTERNAL COUPLING	11
2.1	Induced Current on Shield Exterior	12
2.2	Field Penetration through the Cable Shield	19
CHAPTER 3	INTERNAL CABLE ANALYSIS	24
3.1	Twisting of a Twisted-Pair Cable	24
3.2	MCTLT and the Unevenly Distributed Twist	32
CHAPTER 4	CONCLUSION	40
REFERENCES	42
AUTHOR'S BIOGRAPHY	44

CHAPTER 1

INTRODUCTION

1.1 Background

The following two sections describe one approach for instrumentation, cabling and sensing for impedance measurements. The goal of this thesis is to analyze noise originating in the cables between embedded sensors and the probe electronics. In Section 1.2, one type of impedance instrument and embedded sensing method is described. In Section 1.3, the prototype cabling is described in detail.

1.2 MWM Measurement Method

The JENTEK Sensors 39-channel parallel-architecture impedance instrument system is pictured in Figure 1.1. The sensor for the JENTEK impedance measurement system is the patented Meandering-Wandering Magnetometer (MWM[®] is a registered trademark of JENTEK Sensors Inc.). A generic MWM sensor construct is shown in Figure 1.2 (left). The MWM sensor consists of a meandering primary winding (a modified, patented, winding construct [1]) which when driven with a sinusoidal current, couples through the material under test (MUT) to induce a voltage on the sense elements [2]. The MWM design was adapted for accurate sensor response modeling so that absolute property measurements (e.g., electrical conductivity and magnetic permeability for metals) can be determined using a model-based inverse method [3-6] without calibration standards (see ASTM Standard E2338). An MWM

sensor is typically printed on a flexible material such as Kapton. The number of sense elements and their layout are designed to maximize performance on an application by application basis. All measurements done in this work were made with a 7-channel FA116 which can be seen in Figure 1.2 (right).

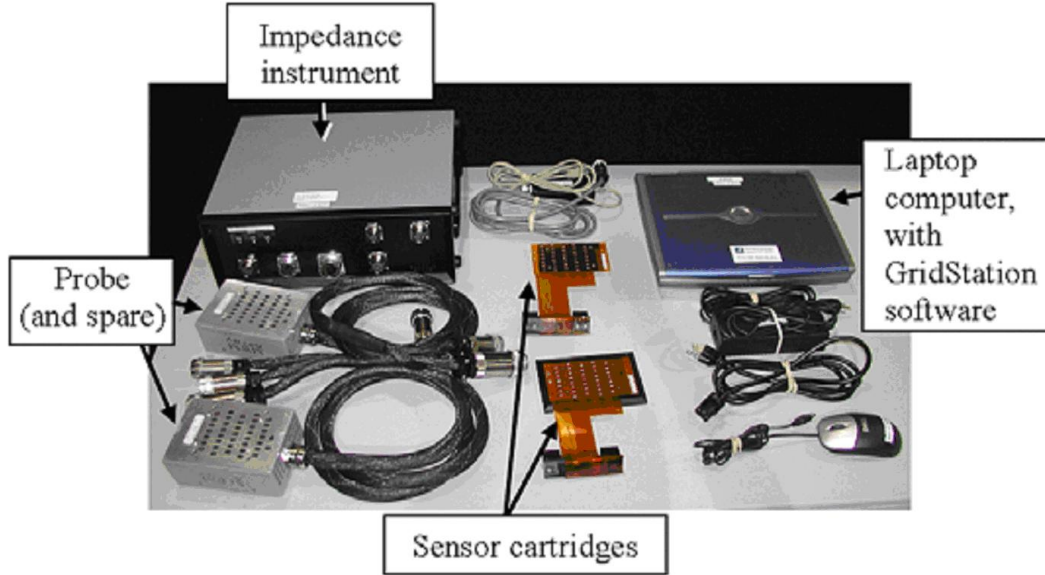


Figure 1.1: Components of a JENTEK Sensors impedance instrument.

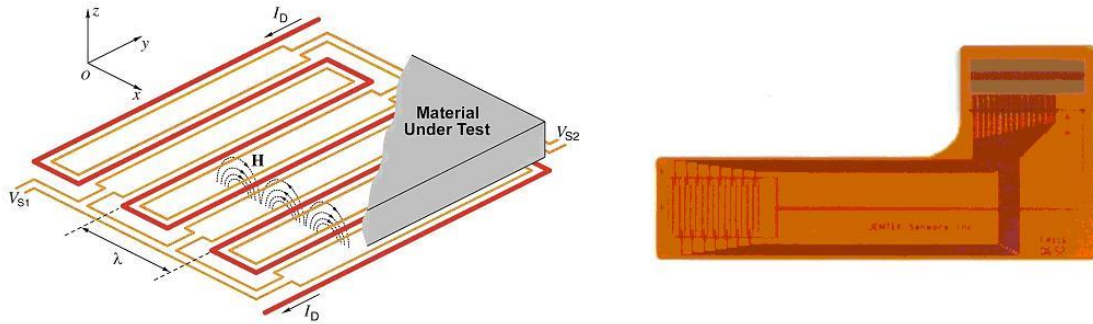


Figure 1.2: Generic MWM sensor schematic (left) and FA116 sensor (right).

The quantities measured by the JENTEK impedance system are the real and imaginary parts of the complex transinductance (impedance/ $j\omega$),

$$\text{Transinductance} = \frac{V_S}{j\omega I_D} = \text{Re}\left(\frac{V_S}{j\omega I_D}\right) + j\text{Im}\left(\frac{V_S}{j\omega I_D}\right) \quad (1.1)$$

where V_S is the voltage across the sense element and is the current exciting the drive winding. Both of these quantities are measured at the probe electronics unit. The impedance system uses a parallel architecture capable of making measurements for 37 channels simultaneously.

The second component of the JENTEK impedance system is the probe electronics unit, which provides several important functions including conditioning the instrument terminals to make them compatible with the sensor terminal characteristics. The probe provides signal conditioning for the sensing elements, which includes amplification, buffering, and filtering of the signals. This is important because the low-level signals found at the sensor terminals can easily be contaminated by loading and parasitic coupling within the cabling to the instrument. The electronics that perform these functions can be seen in Figure 1.3.

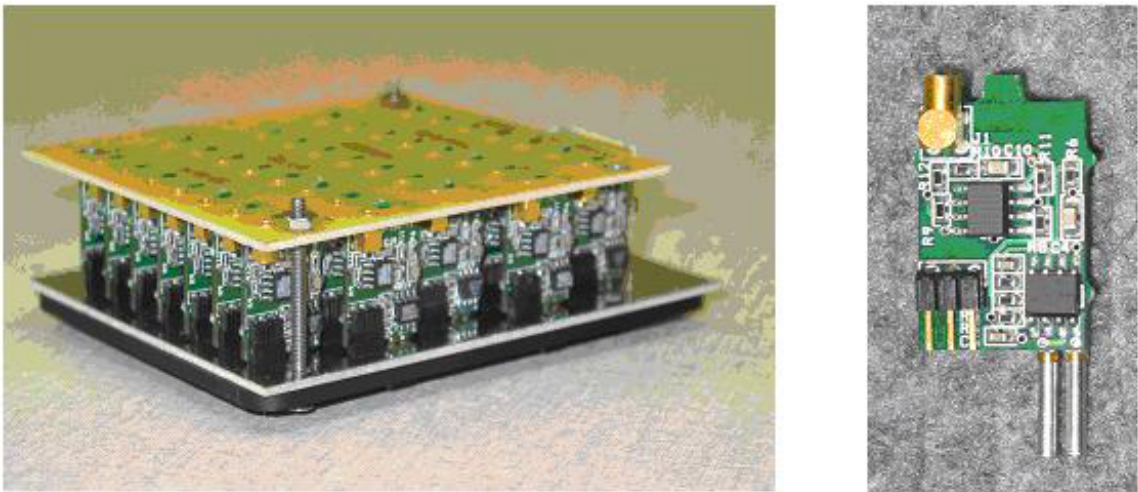


Figure 1.3: Signal conditioning electronics for 37-channel array probe composed of 37 signal conditioning modules in a common backplane structure (left) and single-signal conditioning module (right).

After the sensor signal has been conditioned by the probe electronics and interpreted by the instrument, measured transinductance is converted into absolute material properties by JENTEK's Grid Methods. The Grid Methods use pre-computed

databases of sensor responses to represent the MWM field interactions with the MUT. In this thesis we will limit our discussion to “two-unknown” methods, though these methods have been used with multi-frequency measurements for three unknowns (lattices) and four or more unknowns (hyperlattices).

Figure 1.4 shows a measurement grid for a two-unknown permeability/lift-off measurement at a given frequency, where lift-off is the distance between the sensor and the MUT. The measurement grid is generated using a model of the MWM field interactions with the neighboring material. The model used for this purpose was developed in the 1980s and refined over the years to enable extremely accurate representation of the MWM field interactions. The grid is generated once (off-line) and stored as a pre-computed database for access by the GridStation software. To generate the grid, all combinations of properties (in this case lift-off and magnetic permeability) over the dynamic range of interest are inputted into the MWM models to compute the corresponding grid points in complex transimpedance space. Measurements are then made and run through non-linear search algorithms, resulting in an absolute property measurement. Given an appropriate sensor construct and frequency, a single frequency measurement is capable of independently determining two unknown absolute properties because two quantities are measured, the real and imaginary components of the transimpedance. The measurements plotted in Figure 1.4 were taken on the same material at varying lift-offs. Therefore, it makes sense that the data follows a constant permeability line.

1.3 Prototype Cabling

For some applications, the MWM sensor array is connected directly with the probe electronics unit, seen in Figure 1.1, which performs the measurements of the drive current and sense voltage as well as signal amplification and filtering. However, many

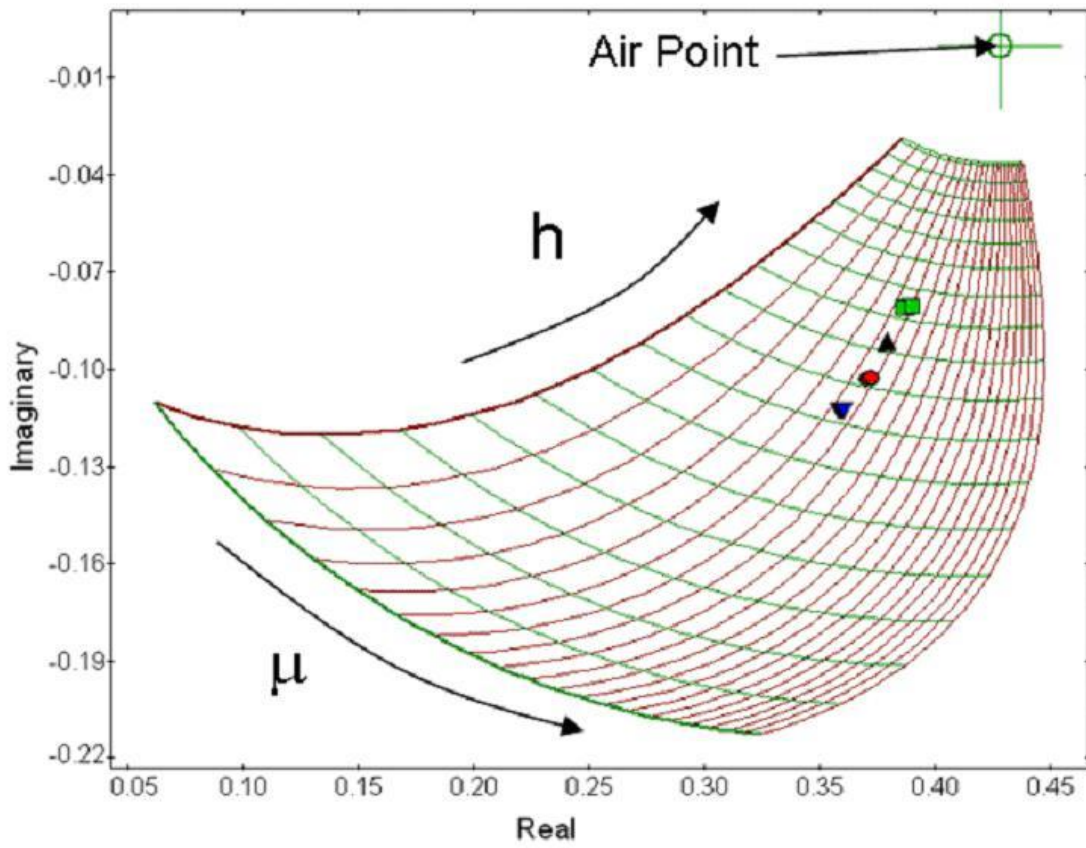


Figure 1.4: Measurement grid for lift-off and magnetic permeability at one applied frequency $f = \omega/2\pi$.

applications do not allow the probe electronics unit to be in close proximity to the MUT and, therefore, cabling is required to connect the MWM voltage sense elements and drive to the appropriate pins on the probe electronics unit. In those applications that require frequencies into the MHz, the cable appears to be a significant source of noise.

This thesis evaluates one cable configuration that is being considered by JENTEK for embedded sensor systems. The prototype cable consists of two shielded twisted-pair wire bundles encased in a flexible, non-conducting mesh. The first shield encases only the drive twisted pair, while the second carries a twisted pair for each sense element used in the application. In applications where multiple sense elements are required, a separate smaller shield is often placed around each sense element in order to minimize cross-coupling between the channels. Figure 1.5 shows the example single-channel cable that connected the FA116 to the probe electronics unit in the measurements taken for this study. At first, only one channel was used in order to limit the number of possible noise-sources examined. Measurements were also taken with a three-channel version of the cable, and these measurements will be used in future analyses.

Figures 1.6 and 1.7 display measurements taken with an FA116 connected to the probe electronics unit through the single-channel cable seen in Figure 1.5. The data is plotted by set, where a set is the average of 100 measurements. Each set acquisition started 60 seconds after the previous, enough time to reposition the cable if necessary. All measurements were taken with no electrical or magnetic conducting material in proximity of the sensor. This was ensured by encasing the sensor in plastic. To eliminate the possibility of a shaky connection between the cable and the sensor, the cable-to-sensor connectors were secured in position with screws. The only variations in the measurements taken in Figures 1.7 and 1.6 are shape changes made to the cables. These shape changes include deflections, looping and twisting of the cable.

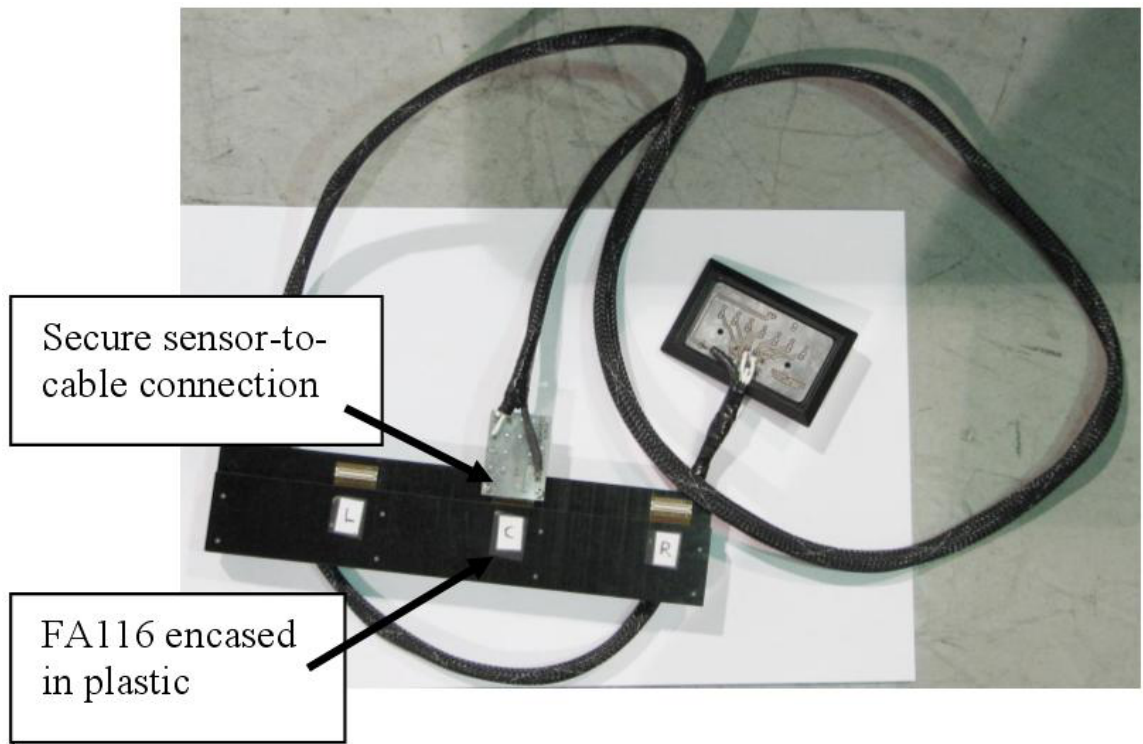


Figure 1.5: Cable connecting probe electronics unit to FA116 sensor in benchtop tests.

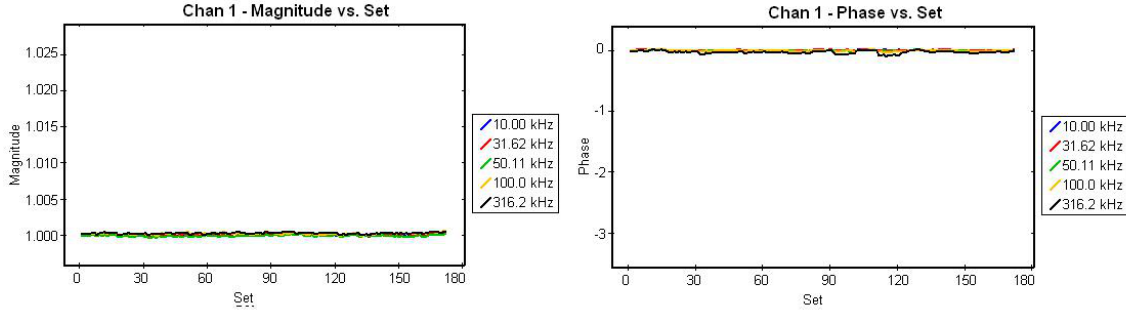


Figure 1.6: Magnitude and phase of impedance measurements taken in air at frequencies from 10 kHz to 316 kHz with cable deflected and twisted.

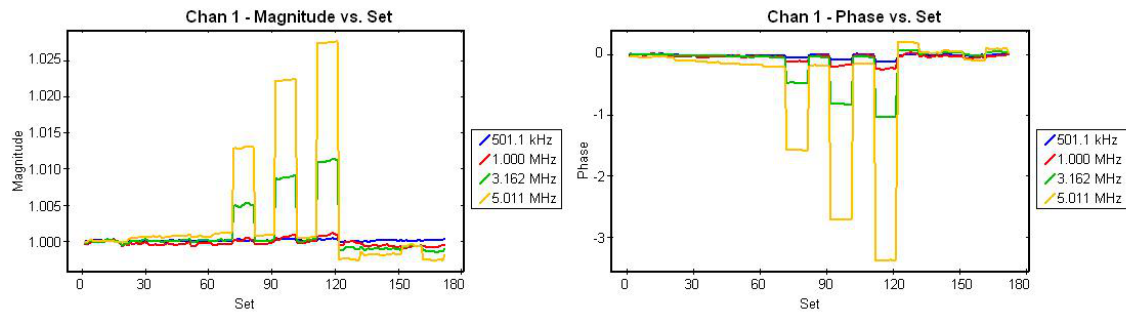


Figure 1.7: Magnitude and phase of impedance measurements taken in air at frequencies from 500 kHz to 5 MHz with cable deflected and twisted.

Figure 1.6 displays the low-frequency measurements and Figure 1.7 displays the high-frequency measurements.

Measurements were also made introducing temperature variations along the cables. The low-frequency and high-frequency measurements are displayed in Figures 1.8 and 1.9 respectively. The temperature ramp during sets 30-40 was approximately 35 °F from 70 °F to 105 °F.

Comparing Figure 1.6 and 1.7, and Figures 1.8 and 1.9, it is clear that varying either the cable shape or the cable temperature introduces variation into the impedance measurement, notably at the higher frequencies. The measurements recorded in Figure 1.6 through 1.9 raise some serious questions:

1. What is the mechanism that causes the change in impedance in the above cases?

- More importantly, is there anything about the cable design that can be altered to lessen the observed variation?

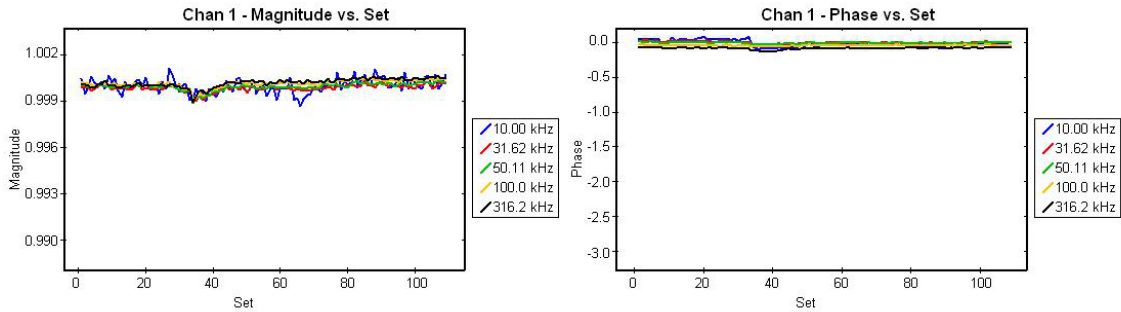


Figure 1.8: Magnitude and phase of impedance measurements taken in air at frequencies from 10 kHz to 316 kHz with cable temperature raised 35 °F during sets 30-40.

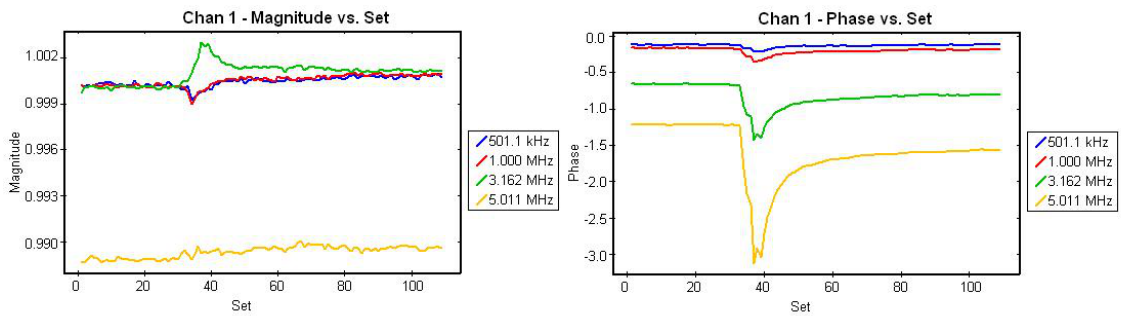


Figure 1.9: Magnitude and phase of impedance measurements taken in air at frequencies from 500 kHz to 5 MHz with cable temperature raised 35 °F during sets 30-40.

A 3% shift in the real component of impedance around the air point, caused by cable shape changes, can be devastating to the accuracy of the measurement, often accounting for more than a 3% shift in the measured property value. Depending on the shape of the measurement grid, which is determined by the geometry of the sensor and the measurement application, a 10% shift around the air point can translate into a huge shift in the absolute properties of a material. For example, assume that a sensor similar to the FA116 is being used to measure the 30% IACS conductivity

(International Annealed Copper Standard) of an aluminum sample at 0.01 inches away from the aluminum at a frequency of 1 MHz. A positive shift in the real component of impedance of the magnitude discussed above would result in a measured conductivity of 60% IACS at an estimated lift-off of 0.015 inches. This measurement would be unrepresentative of the measured sample.

The remainder of this thesis is a study of the impedance measurement noise originating from the prototype cable connecting the MWM sensor array to the probe electronics unit. This analysis is split into two main sections, each covered in a chapter. Chapter 2 presents the analysis of the electromagnetic coupling through the cable shielding between the cable and the outside world and between the conductors within the cable. Chapter 3 examines the impact of changing a cable's shape on its impedance, with emphasis on considering the effect of changing a twisted pair's twist period.

CHAPTER 2

CABLE SHIELDING AND EXTERNAL COUPLING

The tinned copper-braid shield is supposed to isolate the drive and sense twisted-pairs from outside electromagnetic radiation as well as from coupling with each other. The sufficiency of the shielding has not been verified for the prototype cabling.

The approach taken in this study is theoretic because no measurements were available with a known electromagnetic source radiating in the presence of a cable during measurement acquisition. Furthermore, for many embedded sensor applications, it is necessary to show that the cable's shielding is sufficient for measurements in the presence of strong electromagnetic radiation over a wide frequency range from in-flight equipment such as radars. Without access to a high-powered radar, a theoretic approach is appropriate.

This problem can be tackled through a two-step approach, each step aimed at answering one of the following two questions:

1. What is the relationship between incident electromagnetic radiation and the magnitude of the current density induced on the shield exterior?
2. How does the induced current density on the shield exterior translate into a current density on the shield interior, which would then degrade the signals being sent down the shielded wires?

These two questions are addressed next.

2.1 Induced Current on Shield Exterior

The problem of estimating the current density induced on the exterior of the cable shields due to an incident electromagnetic wave can be modeled approximately in terms of the calculation of a uniform plane wave interaction with a thin, straight wire. Figure 2.1 shows the geometry of the problem. It consists of a thin wire of length l and circular cross section of radius r , centered at the origin and with its axis in the z -direction. An electromagnetic plane wave with angular frequency ω propagates with a wave vector \hat{k} at an angle θ_{inc} to the z -axis.

A thin wire approximation is understood to mean that, given a wire with radius r much smaller than the incident wavelength, current is only induced along the wire's main axis (in this case, the z -direction). Furthermore, the current is uniformly distributed around the circumference of the wire. Therefore, the current magnitude and phase are only a function of z . This is assumed to be a valid approximation as long as $l \gg r$ and $\omega r \ll c$, where c is the speed of light [7]. Given that the typical shield radius of concern is 0.0032 - 0.0064 m and that the typical cable length is 1 - 2 m, the first condition is satisfied. And, given that the frequencies of interest are less than 50 MHz, the second condition is also satisfied.

Before approaching the induced current density problem, a useful and informative exercise was to show that the thin wire approximation is valid for the problem at hand given the geometric aspect ratios and the frequency range of interest. This was accomplished using the two-dimensional finite element method (FEM) analysis of plane wave scattering by a cross-section of an infinitely long conducting cylinder in free space. The incident plane wave was assumed to be normally incident on the cylinder aligned in the z -direction and to have a TM-polarization so that the electric field only has a z -component. Validation of the FEM code was achieved by comparing it to an analytic solution for the case of a normally incident TM plane wave found in

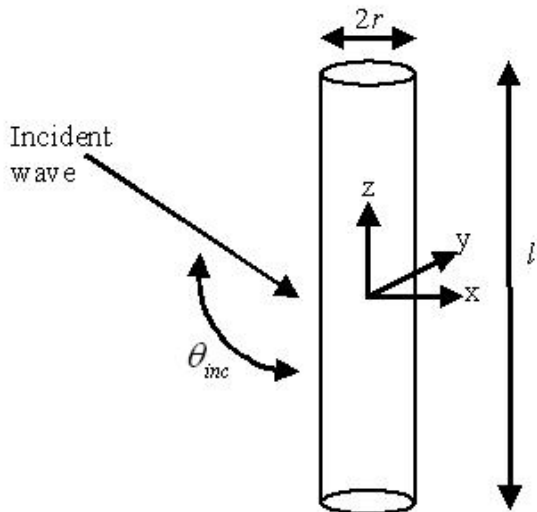


Figure 2.1: Geometry of the thin-wire scattering problem.

Balanis [8]:

$$E_z^{sc}(r, \theta) = -E_0 \sum_{n=-\infty}^{\infty} \frac{J_n(\beta a)}{H_n^2(\beta a)} H_n^2(\beta r) e^{jn\theta} \quad (2.1)$$

where a is the radius of the cylinder. The wavelength to radius of cylinder ratio was set to 10 and 20 for a unit circle cylinder. For all results in this section, the characteristic mesh size was set so that there were at least 20 elements-per-wavelength. The results can be seen in Figure 2.2.

With the FEM simulation code validated, it can be used for the validation of the thin-wire approximation. Since the induced surface current should only be in the z -direction and uniformly distributed around the wire if the thin-wire approximation is valid, the scattered field in the xy -plane should be radially symmetric. For practical applications, it becomes necessary to know at what wavelength-to-radius ratio this approximation breaks down. The scatterer in question, as mentioned previously, is the No. 36 American wire gauge (AWG), which has a radius of 0.000127m.

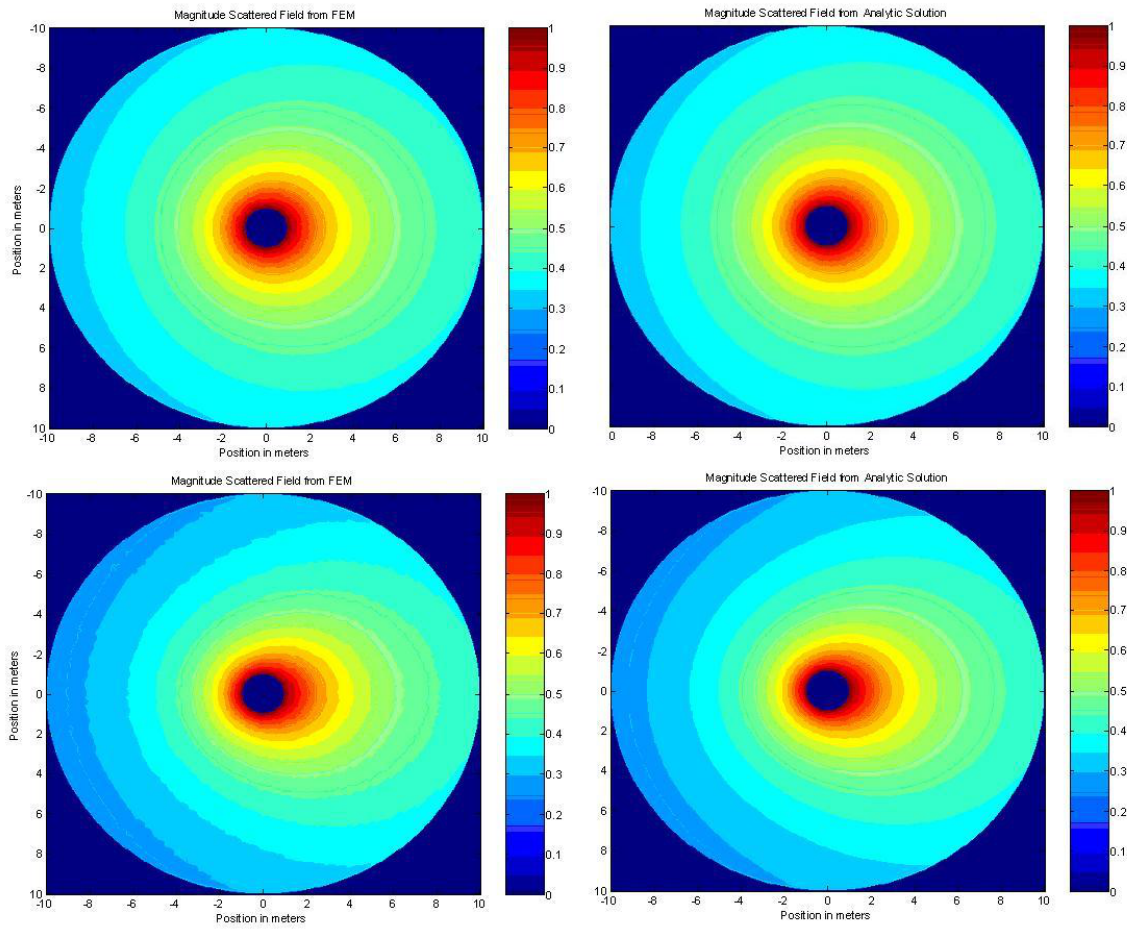


Figure 2.2: FEM TM-polarization scattered field results (left) and analytic scattered field results (right) for wavelength to radius of cylinder ratio of 20 (above) and 10 (below).

Figure 2.3 contains TM polarizations for wavelength-to-radius ratios of 200, 100, 50, 25, 20 and 10. Visually it is clear that the approximation breaks down when the wavelength of the incident wave is between 25 and 50 times the size of the radius of the scatterer. Therefore, a good rule of thumb for the thin wire approximation is that the incident wavelength is greater than 50 times the radius of the wire.

The geometry of the problem of estimating the current density induced on the cable shield due to incident electromagnetic wave lends itself well to a moment method solution and has been studied theoretically in the context of scattering of radar signals by wires dropped from airplanes [9]. The validity of this solution has also been verified experimentally [10]. As validated above, the thin wire approximation states that the induced surface current \vec{J}_z is uniform around the conductor's circumference and is only in the z-direction. Therefore, it can be expressed as

$$\vec{J}_z(\vec{r}) = \hat{z} \frac{I(z)\delta(\rho - r)}{2\pi r} \quad (2.2)$$

where $I(z)$ is the current as a function of position along the z-axis, which is valid from $-l/2$ to $l/2$.

The easiest way to solve for the electric field due to the induced surface current is to first solve for the Lorenze gauge vector potential, which, due to a time-harmonic current, can be expressed in phasor form as

$$\vec{A}(\vec{r}) = \frac{\mu_o}{4\pi} \int \vec{J}(\vec{r}') \frac{\exp(-jk|\vec{r} - \vec{r}'|)}{|\vec{r} - \vec{r}'|} d^3r' \quad (2.3)$$

In terms of \vec{A} , the electric field is expressed as

$$\vec{E}(\vec{r}) = -jck\vec{A}(\vec{r}) + \frac{jc}{k}\vec{\nabla}[\vec{\nabla} \cdot \vec{A}(\vec{r})] \quad (2.4)$$

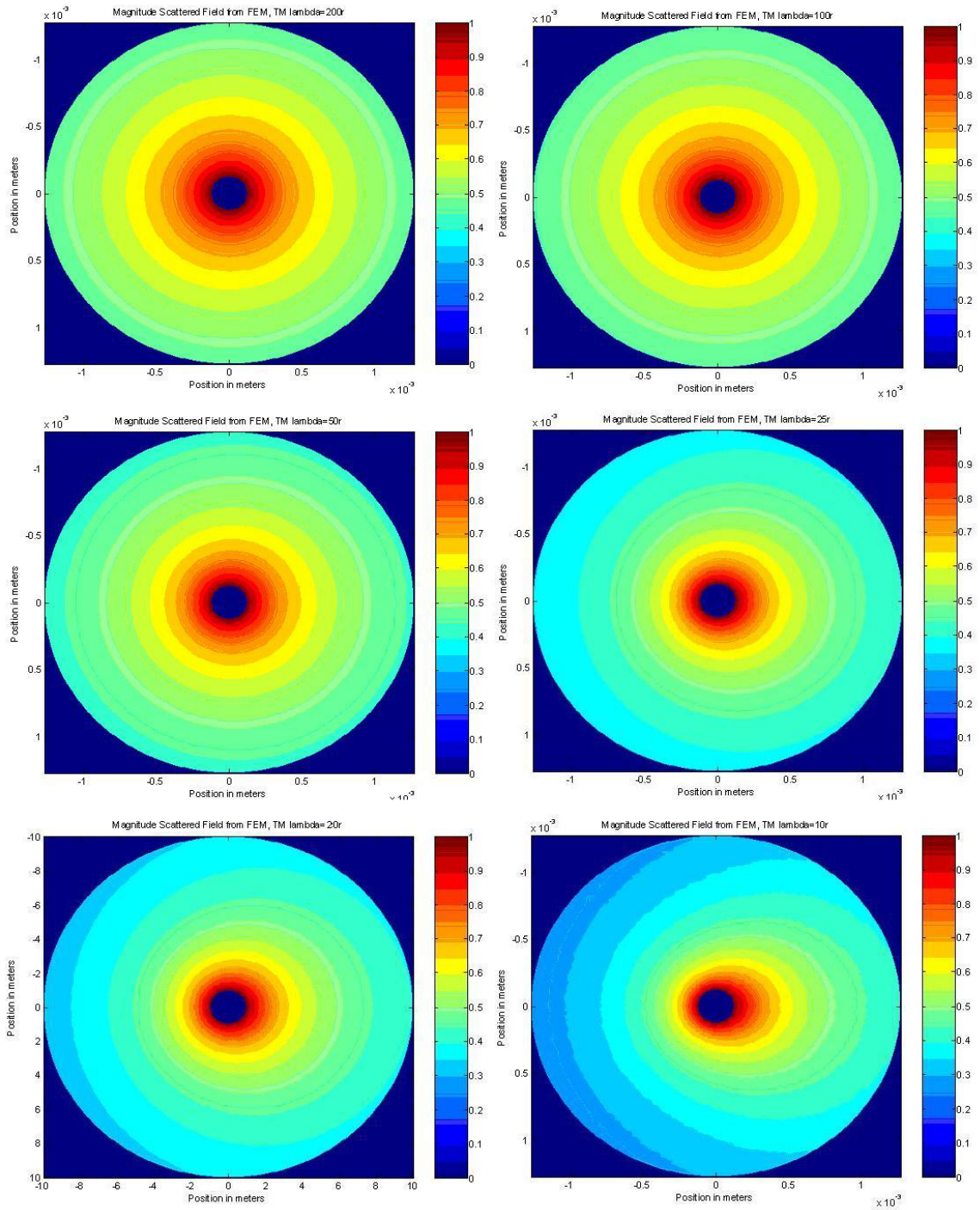


Figure 2.3: FEM TM-polarization scattered field results for wavelength to radius of cylinder ratio of 200, 100, 50, 25, 20 and 10 (from top to bottom, left to right).

Evaluating the field at the surface of the conductor, we have

$$E_z(\rho = r, z) = \frac{jc}{k} \left(\frac{\partial^2}{\partial z^2} - k^2 \right) A_z(\rho = r, z) \quad (2.5)$$

For a computable expression of the z-component of the Lorenze gauge vector potential, we take (2.3) and evaluate at the surface of the conductor, getting

$$A_z(\rho = r, z) = \frac{\mu_o}{4\pi} \int_{-l/2}^{l/2} I(z') K(z - z') dz' \quad (2.6)$$

where the kernel K is expressed as

$$K(z - z') = \frac{1}{\pi} \int_0^\pi \frac{\exp\left(-jk\sqrt{(z - z')^2 + 4r^2 \sin^2(\beta)}\right)}{\sqrt{(z - z')^2 + 4r^2 \sin^2(\beta)}} d\beta \quad (2.7)$$

Equations (2.5)-(2.7) provide the electric field radiated due to the induced surface current on the conductor. Our perfect electrical conducting (PEC) boundary condition states that the sum of this field and the z-component of the incident field must evaluate to zero at the surface of the conductor. Since we can approximate the z-component of the incident field at the surface of the conductor as the average of the z-component of the incident field around the wire due to the thin wire approximation, we can construct a set of linear equations with the induced surface currents as the unknowns.

To accomplish this, we first must define a set of basis functions for the expansion of the induced surface current. Piecewise sinusoidal basis functions are appropriate since they allow for some of the integrations to be solved analytically.

$$F_n(\vec{r}) = \frac{\delta(\rho - r)}{2\pi r} \begin{cases} \frac{\sin(k|z - z_{n-1}|)}{\sin(k|z_n - z_{n-1}|)} & z_{n-1} < z < z_n \\ \frac{\sin(k|z - z_{n+1}|)}{\sin(k|z_n - z_{n+1}|)} & z_n < z < z_{n+1} \\ 0 & \text{otherwise} \end{cases} \quad (2.8)$$

where z_0 and z_{N+1} are the ends of the cylinder and n runs from 1 to N with

$$z_n = \frac{nl}{N+1} - \frac{l}{2} \quad (2.9)$$

The one-dimensional basis functions can be expressed as

$$f_n(z) = \begin{cases} \frac{\sin(k|z-z_{n-1}|)}{\sin(k|z_n-z_{n-1}|)} & z_{n-1} < z < z_n \\ \frac{\sin(k|z-z_{n+1}|)}{\sin(k|z_n-z_{n+1}|)} & z_n < z < z_{n+1} \\ 0 & \text{otherwise} \end{cases} \quad (2.10)$$

Using the basis functions we can construct the current density induced on the wire surface as

$$\vec{J}(\vec{r}) = \hat{z} \sum_{n=1}^N I_n F_n(\vec{r}) \quad (2.11)$$

where I_n is the current at z_n .

Next, let us define V_n as the field produced at the n th segment by a unit amplitude incident field in the direction of \hat{E}_0 . Therefore,

$$V_n = \frac{\hat{E}_0 \cdot \hat{z}}{2\pi} \int_0^{2\pi} d\phi \int_{z_{n-1}}^{z_{n+1}} f_n(z) e^{ikz \cos \theta_{inc}} e^{ikr \cos \phi \sin \theta_{inc}} dz \quad (2.12)$$

By the PEC boundary condition this V_n term must cancel with the average field from all current segments along the wire. This condition results in a system of N equations with N unknowns $\{I_m\}$.

$$V_n = \sum_{m=1}^N Z_{nm} I_m \quad (2.13)$$

Z_{mn} can be called an impedance matrix, and the (m, n) entry can be expressed as

$$Z_{nm} = \int_{z_{m-1}}^{z_{m+1}} dz \int_{z_{n-1}}^{z_{n+1}} dz' K(z-z') \left(\frac{j}{k} f'_m(z) f'_n(z) - jk f_m(z) f_n(z') \right) \quad (2.14)$$

The above equations are straightforward to implement in Matlab using approx-

imation via mid-point integration. Solving the system for frequencies ranging from DC to 50MHz on a cable ranging in length from 1 to 2 m, ranging in wire diameter from 0.0032 to 0.0064 m, and varying the angle of incidence of the incoming wave, it is possible to get an upper bound on the possible induced current on the outside of the cable shield by an incident electromagnetic plane wave of unit amplitude. The center of a 2 m long cable of diameter 0.0064 m, with a 50 MHz unit amplitude plane wave incident at an angle of $\pi/2$, experiences an induced current density of 0.0036 A/m. This scales directly with the amplitude of the z-component of the electric field. This result can be seen in Figure 2.4. It should be noted that this upper bound assumes that the direction of the polarization of the plane wave is in the xz-plane. So, a $\pi/2$ incident angle places the entire electric field in the z-direction. It should also be noted that this upper bound is only valid in free space and would be lower if the cable were in the presence of other shielded cables (such as a drive shield and sense shield in proximity) or other conducting objects (such as the aircraft itself). Validation of the numeric approach was achieved by comparing the above approach to the analytic result from Balanis [8] of a normal incident TMz plane wave on a long thin wire.

2.2 Field Penetration through the Cable Shield

In [11] Tesche provides the framework to address the second question: How does one translate the current density on the external surface of the shield into a distributed series voltage source (V_s^i) and a distributed shunt current source (I_s^i) on the transmission line created by the internal surface of the shield and the conductor of the twisted pair? He provides the equations

$$V_s^i(z) = Z_t J^e(z) \quad I_s^i(z) = \Omega_t \tau^e(z) \quad (2.15)$$

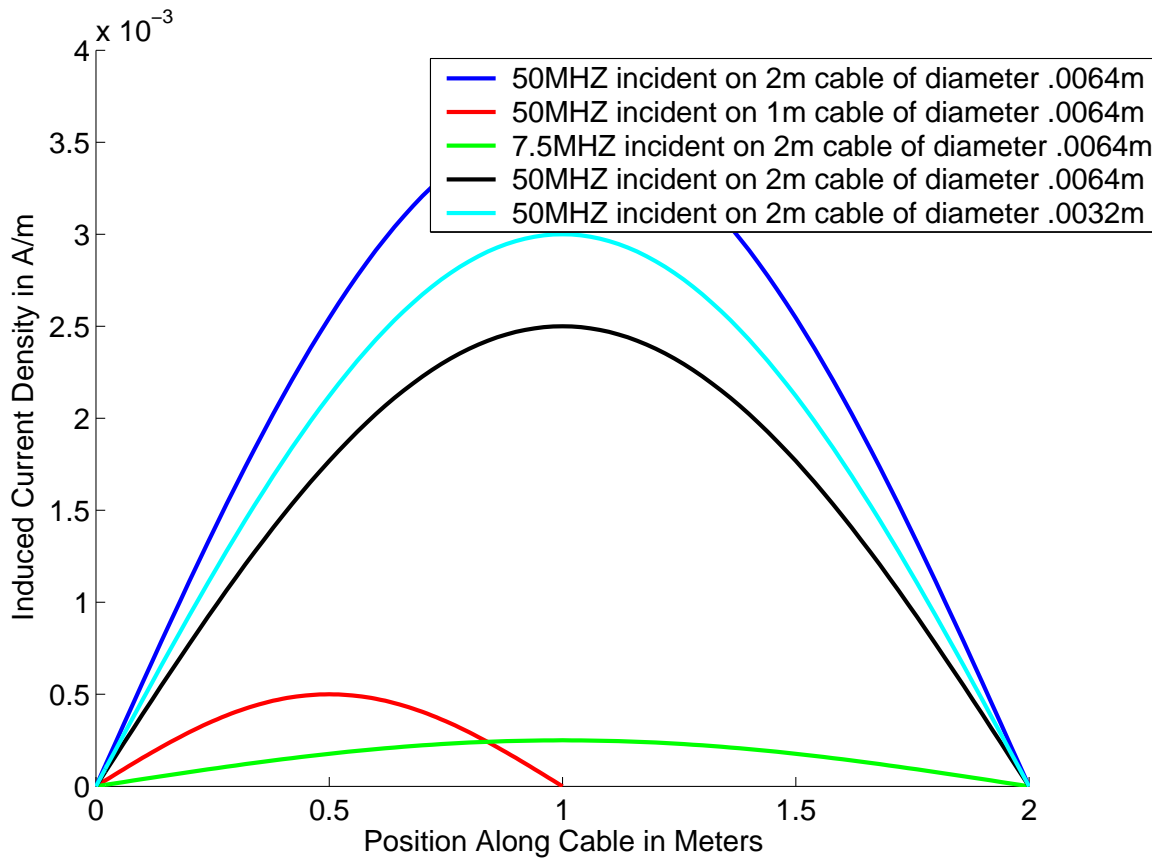


Figure 2.4: Numerically calculated induced currents for varying incident frequencies on cables with varying geometries.

where J^e is the external surface current density, τ^e is the external surface charge density, Z_t is the impedance transfer function, and Ω_t is the charge transfer function.

For a single-layer braided shield, such as the one used in the JENTEK prototype cabling, the impedance transfer function Z_t is given by

$$Z_t(\omega) = R_0 \frac{\gamma d}{\sinh(\gamma d)} + j\omega M \quad (2.16)$$

where M is the inductance leakage of the shield, R_0 is the DC resistance of the shield, d is the diameter of the individual wire strands in the braid and γ is the propagation constant of the shield which can be approximated as

$$\gamma \approx \sqrt{j\omega\mu_0\sigma} \quad (2.17)$$

since the conductivity σ of the copper shield is large.

The charge transfer frequency Ω_t can be expressed as

$$\Omega_t(\omega) = \frac{-j\omega S}{\eta c Z_c} \quad (2.18)$$

where S is the shield leakage parameter and Z_c is the characteristic impedance of the internal transmission line. The twisted pair used for the sense elements has $r = 0.00061$ m and $D = 0.00152$ m, where D is the distance between the center of the wires and r is the radius of the conductors. Comparable commercial shielded pairs with similar dimensions documented in IBM [12] and GORE (a manufacturer of controlled impedance twisted-pair cables) [13] place the characteristic impedance of such a shielded twisted pair between 100 Ω and 150 Ω . So a value of $Z_c = 125 \Omega$ is a reasonable approximation. Given the properties of the copper braid shield used in the JENTEK prototype cables, we have $d = 0.000127$ m, $R_0 = 3.12 \times 10^{-2} \Omega/\text{m}$, $M \approx 0.75 \times 10^{-9}$ H/m and $S \approx 25 \times 10^6$ m/F.

Figure 2.5 displays the magnitude of the transfer functions Z_t and Ω_t over the frequency range of interest for the prototype shield. It should be noted that similar shields with larger internal radii are also used in prototype cables, but that would not affect the transfer functions significantly.

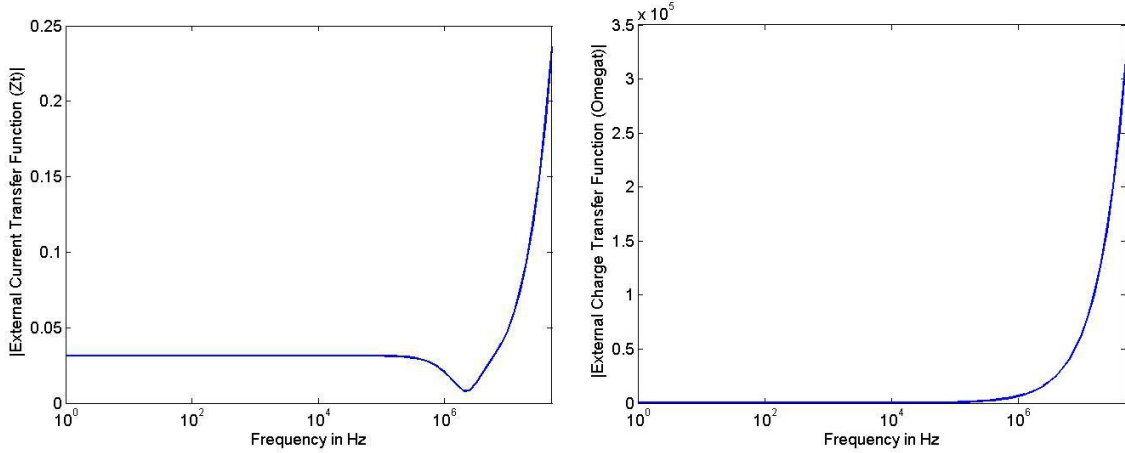


Figure 2.5: Transfer functions of the prototype shield for converting external current to internal distributed series voltage source (left) and for converting external charge density to internal distributed shunt current source (right).

According to [14], aircraft radar can have an average radiated field strength of over 600 V/m for frequencies up to 50 MHz. Therefore, even under conditions only 1% of ideal, a 0.0017 A current could be induced on the prototype shield at 7.5 MHz. According to the Z_t transfer function, this would result in a 40 mV/m distributed series voltage source inside the shield. In general, JENTEK’s sense elements carry a voltage signal of 0.5 mV. So it is immediately clear that in the presence of a strong high-frequency field source such as radar, JENTEK’s prototype cable shielding would not be sufficient. Even though these fields are not necessarily present inside an aircraft, for in-flight validation, and for use around high powered radar, JENTEK should consider increasing their shield strength. An easy way to drastically improve the effectiveness of a braided shield is to double the braided layers. Tesche [11] shows that the Z_t of a double braid has a much more complicated expression but with a

much smaller magnitude and that $\Omega_t \approx 0$ when the two braids are not separated.

In normal applications, however, JENTEK's prototype shields are sufficient. The drive and the sense elements produce low-power radiation that does not escape the shields. External sources that radiate at such high frequencies are rare. In high-frequency applications, lower-frequency noise is filtered out at the probe electronics unit. And at lower frequencies, the amplitude of the current induced on the outside of the shield is orders of magnitude smaller. For example, over the range of cable dimensions stated above, the highest amplitude current excited by a unit amplitude 1 kHz incident field is 1.25×10^{-6} A/m, five orders of magnitude smaller than the field excited by the 50 MHz incident field. Furthermore, the braided shield is more effective at these lower frequencies.

CHAPTER 3

INTERNAL CABLE ANALYSIS

The following analysis focuses on how shape changes affect impedance measurements rather than focusing on the effect of temperature changes. The reason for this is two-fold. First, it requires a rather large temperature variation of 35 °F to create the less than 0.5% impedance shift relative to the air point, compared to the up to 3% impedance shift created by shape changes of the cable at frequencies up to 5 MHz. Temperature variations of this magnitude are rarely seen during measurement acquisition as the environments are normally controlled. Second, even if temperature variations were anticipated, intelligent use of a thermocouple and signal processing could correct for such variations. Furthermore, temperature variations of the cable are much easier to monitor than shape variations.

The analysis also makes the assumption that the twisted pair of the drive is sufficiently decoupled from the twisted pairs of the sense elements. This assumption was validated in the previous chapter. Thus the two shields can be considered independent of one another.

3.1 Twisting of a Twisted-Pair Cable

Taking a closer look at Figure 1.7, and ignoring the gradual drift of the data at the higher frequencies during the first 60 sets (which is a common settling of the system into its steady operating state and occurs with or without a cable), there are a few characteristics worth noting. Over the first 70 sets, test arcs of various sizes

were introduced into the cable: the center of the cable was deflected 10, 20 and then 30 inches, and then an entire loop was formed. These shape variations caused the small data fluctuations observed in Figure 1.7. After data was acquired for each arced position, data was acquired for the straight configuration. One would hope that the measured impedance will return to the baseline whenever the cable is returned to the straight configuration. However, this does not happen, implying that some remnant of the cable shape variation persists even when the cable is returned to the straight configuration.

Another interesting and important characteristic of Figure 1.7 is that the three impedance deviations between sets 70 and 120 are by far the largest. These deviations were created by twisting the cable. In these cases, not only was the original deviation the largest, but the largest variation remained when the cable was returned to its baseline configuration.

These two observations indicate that cable twisting has a larger impact on impedance measurements than other cable distortions. Therefore, cable twisting becomes the important shape variation to study. Not only are the cable parameters the most sensitive to these deformations, but the associated impedance variations are the most persistent; simply untwisting the cable does not return the cable to its original state.

Figure 3.1 is a plot of the effect of twisting on the air point impedance. It shows only the data from the partial and complete twists introduced to the cable and the measurements taken when the cable is straightened out after each twist. The deviations are one-half twist, full twist and one and one-half twists in that order. Clearly, the more the cable is twisted, the more the impedance measurement is affected. And the more the cable is twisted, the more the impedance measurement deviates from the air point after the cable is untwisted.

Geometrically, when a cable containing twisted pairs is twisted, the period of the twisted-pair twist is altered. A full twist in the cable would be distributed along the

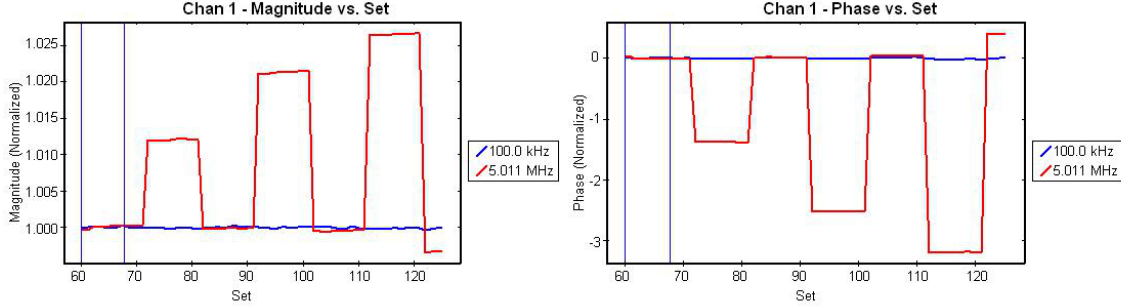


Figure 3.1: Normalized air point impedance measurements made at 100 kHz and 5 MHz when the cable is twisted. Sets 72-81 are with half a twist, 92-101 have a full twist, and sets 112-121 have a one-and-a-half twists. In between the cable is straightened.

cable, altering each twist period slightly. The measurements indicate that altering the twist period affects the higher frequencies much more than the lower frequencies. In fact, frequencies below 300 kHz appear to be unaffected.

It would seem that the easiest solution to this problem would be to eliminate the use of twisted pairs altogether and only use coaxial wires for the sense element cables. However, twisted pairs have the major advantage of being a balanced signal pair. They can carry a differential signal with the conductors having equal impedances along their lengths and equal impedances to ground and the circuitry of the probe electronics unit. This balance allows for good common-mode noise rejection, especially due to the stray electric fields studied in the previous chapter. Measurements have confirmed that the measurement-to-measurement common-mode noise introduced by replacing the twisted pairs by coaxial lines outweighs the benefit of eliminating changes in the twisted-pair period. This is true even with individual shields around each of the coaxial sense-elements, making it effectively a triaxial cable.

A relatively straightforward way to test if changing the twisted-pair period is responsible for the change in impedance measurement is to make measurements with cables that have base twist periods of different lengths. Distributing an extra twist along cables of the same length with different twist periods should have different

results. Using the approximation that the twist is distributed evenly along the cable, we can turn to Lefferson [15] and the expression derived there to calculate the characteristic impedance and effective dielectric constant of a twisted pair:

$$Z_C = \frac{Z_0}{\pi\sqrt{\epsilon_{r,eff}}} \cosh^{-1} \left(\frac{D}{d} \right) \quad (3.1)$$

where Z_0 is the untwisted characteristic impedance, d is the diameter of the conductor in the twisted pair, and D is the outer diameter of the insulating dielectric surrounding the conductor. The effective dielectric constant, $\epsilon_{r,eff}$, can be calculated from the dielectric constant ϵ_r , the twists-per-unit-length T , and D by

$$\epsilon_{r,eff} = 1 + (.25 + .0004 \arctan(T\pi D)^2) (\epsilon_r - 1) \quad (3.2)$$

Normalizing Equation (3.1) and plotting it and its derivative with respect to T , we get Figure 3.2. The plot of the derivative of the characteristic impedance indicates that if the impedance measurement deviations were in fact caused by changes in the impedance of the cable, adding an extra twist would cause more of an impedance deviation the tighter the twist, until approximately 10 twists-per-inch. This is basically what we see in the left plot of Figure 3.3. Cables were constructed that have approximate twist period of 4, 6, 9 and 12 twists-per-inch. The current JENTEK prototype cable has twist period of 6. Cables with twist periods of less than 4 twists-per-inch were difficult to construct with a consistent period due to the looseness of the twist, and cables with twist periods of greater than 12 were difficult to construct due to the stress of twisting on the conductors. The impedance deviation due to a twist in the cable was measured 10 times, with each twist in the direction that would loosen the twist.

Interestingly enough, the measured impedance response due to bending of the cable behaved similarly to that of the measured impedance response due to twisting

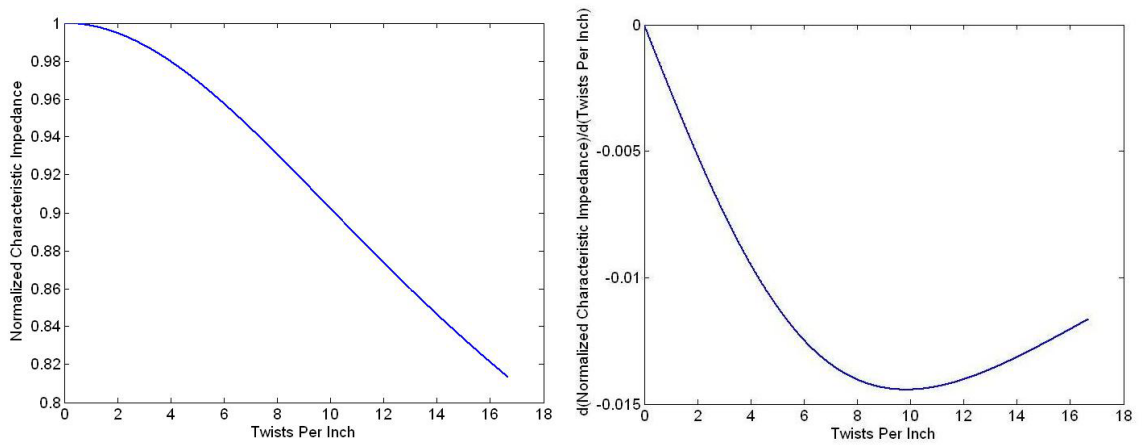


Figure 3.2: Normalized characteristic impedance versus number of twists-per-inch of a twisted pair (left). Derivative of the normalized characteristic impedance with respect to number of twists-per-inch (right).

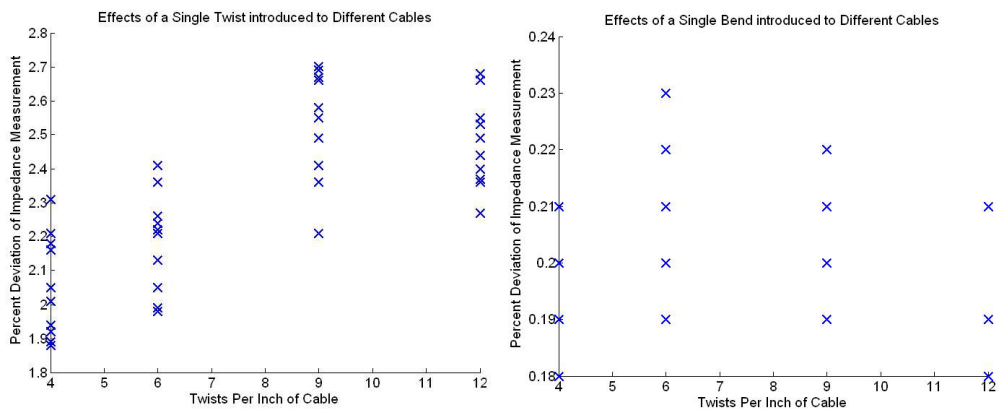


Figure 3.3: Impedance change due to a single twist in the loosening direction for cables of different twist periods (left). Impedance change due to a single bend introduced to cables of different twist periods (right).

of the cable. These results can be seen in the right plot of Figure 3.3. This seems to imply that bending a cable causes measurement shifts because it alters the twist period of the twisted pair, only causing smaller impedance shifts than those that occur when the cable is actually twisted. Therefore, the analysis of the twisting of the cable is generalizable to the bending of the cable as well.

From Figure 3.3 it is clear that altering the period of the twisted pairs in the JENTEK prototype cables is not the solution to the problem. Decreasing the period only lessens the impedance shift slightly before it becomes difficult to maintain a stable twist period, and such a loose twist would start to degrade the benefits of the balanced differential line. Increasing the twist period has potential benefits, but physical limitations prevent the twist from being tight enough to realize these benefits. Therefore, it becomes necessary to look a little closer at the mechanism by which the altered characteristic impedance of the cable affects the impedance measurement of the MWM sensor.

Figure 3.4 shows how the drive current and sense voltage are independently affected by the cable twist in the loosening direction. Loosening the twist of the cable raises its characteristic impedance, causing the magnitude of the voltage-controlled drive current to drop. Ignoring other factors, the voltage on the sense elements drops since the induced voltage on the sense element is directly proportional to the magnitude of the sinusoidal drive current. These factors cancel each other out when dividing and computing the transimpedance. However, the induced voltage on the sense element actually rises when a twist is introduced to the cable. This is because the rise in the cable's characteristic impedance raises the impedance load on the sense element. This rise in the characteristic impedance of the sense element cable and resulting rise in the induced voltage on the sense element is what drives the shift in measured impedance.

A calculation can verify if the changing of the characteristic impedance due to

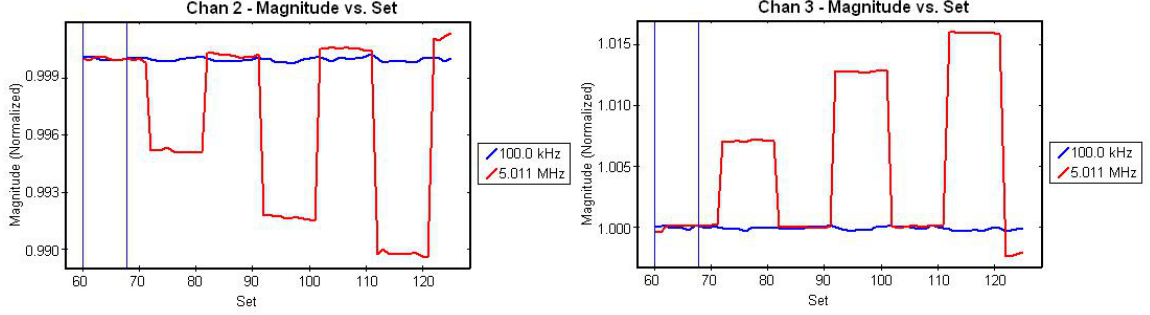


Figure 3.4: Change in the magnitude of the drive current due to twisting of the prototype cable in the loosening direction (left) and change in the magnitude of the sense element voltage due to twisting of the prototype cable in the loosening direction (right). These measurements are the same as in Figure 3.1.

a loosening twist could be responsible for the shifting of the induced sense element voltage by the 2% observed. First, since the characteristic impedance of the twisted pair was defined relative to the untwisted or twin-lead cable, the following equation for the characteristic impedance of a twin-lead cable is needed:

$$Z_0 = \frac{377}{\pi\sqrt{\epsilon_r}} \cosh^{-1} \left(\frac{R}{d} \right) \quad (3.3)$$

Here R is the distance between the center of the conductors and d is still the diameter of the conductor. Given the conductors and insulation used in the twisted pairs, $Z_0 = 121.5 \Omega$. At six twists-per-inch, the characteristic impedance would be decreased by a factor of 95.73%. So, $Z_C = 116.31 \Omega$. One twist in the loosening direction distributed along the 1 meter long cable results in a cable with 5.97 twists-per-inch. This changes the characteristic impedance to 117.1Ω .

The following equation can be used to calculate the induced voltage on the sense element by the drive current I_D . It is derived from applying the Kirchoff voltage law to the circuit loops in Figure 3.5.

$$V_{sense} = \frac{j\omega M I_D}{j\omega L_{sense} + Z_L} Z_L \quad (3.4)$$

In Equation (3.4), ω is the frequency of the sinusoidal drive current, M is the mutual inductance between the drive and sense loops, Z_L is the impedance loading the sense element (due to the cable and its termination in the probe electronics unit) and L_{sense} is the inductance of the sense element loop of wire. L_{sense} can be approximated by the following equation [16]:

$$L_{sense} = \frac{2W\mu_0}{\pi} \ln\left(\frac{W}{a} - 0.77401\right) \quad (3.5)$$

where W is the width of the rectangular loop of wire of the sense element, and a is the wire radius used to create the sense element.

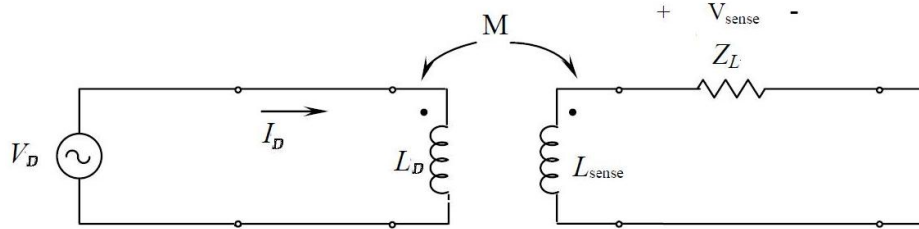


Figure 3.5: Equivalent circuit representing drive winding and sense element coupling that is used to derive Equation (3.4).

Given how the JENTEK prototype cable is terminated in the probe electronics unit, we can use Equation (3.4) and take the ratio of the induced sense voltage for the characteristic impedances before and after the loosening twist is introduced. It should be noted that it is never necessary to calculate M since it cancels when the ratio is taken. At 5 MHz, this results in an increase in the magnitude of V_{sense} by 1.02%. This is on the same order as the 2% errors observed at 5 MHz. The discrepancy is in part due to the poor assumptions that the twist is distributed evenly along the cable and that the electrical length of the line does not change due to the distributed twist. This is also the cause for the uncertainty in the error in Figure 3.3. These assumptions will be addressed in the next section.

3.2 MCTLT and the Unevenly Distributed Twist

To more accurately model and understand how the changing of the impedance measurement across frequencies is due to changing of the cable’s characteristic impedance, we must turn to a method that does not require the invalid assumption that the twist is evenly distributed along the cable. The tool used for modeling the internal design of this JENTEK prototype cable was developed in Professor Andreas Cangellaris’ research group and is called the Multi-Conductor Transmission Line Tool (MCTLT). MCTLT uses a geometrical description of the cable (length, diameter, number and placement of the conductors and shield, etc.) and a property description of the materials to efficiently calculate the matrix-based Green’s functions commonly used for multi-wire cable analysis. Specifically it calculates the matrices $G(d, \omega)$, $G_z(d, \omega)$, and $G_y(d, \omega)$ which are defined as follows:

- $G(d, \omega)$: the propagator from a physical series voltage source to a physical voltage wave amplitude, traveling away from the source and at a distance d from the source, at angular frequency.
- $G_z(d, \omega)$: the propagator from a physical shunt current source to a physical voltage wave amplitude, traveling away from the source and at a distance d from the source, at angular frequency.
- $G_y(d, \omega)$: the propagator from a physical series voltage source to a physical current wave amplitude, traveling away from the source and at a distance d from the source, at angular frequency.

In the above descriptions, the word “physical” means that it can be measured as the difference between a signal conductor and the reference conductor. In order to efficiently calculate the above matrix-based Green’s functions, an intelligent stable rational function expansion is employed. Other useful matrices that are computed

are the per unit length (pul) resistance, conductance, inductance and capacitance matrices.

Since it was shown in the previous section that the driving factor causing impedance measurement variation is the change in characteristic impedance of the sense elements due to cable twisting, the pul matrices for resistance, conductance, inductance and capacitance matrices will be especially useful. They can be used, along with the following formula, to determine the characteristic impedance at different frequencies of different length twisted pairs with different twist periods.

$$Z_0 = \sqrt{\frac{R + j\omega L}{G + j\omega C}} \quad (3.6)$$

Figure 3.6 shows the characteristic impedance of a twisted pair as a function of frequency for a few different twist periods, as calculated by MCTLT. As the frequency increases, the difference in the characteristic impedance of the twisted pairs also increases. This is one factor which leads to higher measurement variation due to twisting at higher frequencies.

Since MCTLT is only capable of modeling twisted-pair cables with constant twist periods, the characteristic impedance of individual twist periods of different lengths must be used to construct the characteristic impedance of a longer twisted pair with a varying twist period. Originally the thought was to turn to [17] in which Kissel lays out the framework for which localization theory could be applied to the problem of modeling a twisted pair with a probabilistically varying twist period. Kissel applies the work of Furstenberg's theorem for the product of independent, identically distributed, random matrices and numeric methods of calculating the upper Lyapunov exponent to the problem of an infinitely long disordered mass spring chain. If the varying period did not have certain constraints on it, this problem would have had direct parallels with the problem of calculating the matrix Green's functions of a probabilistically varying period of a twisted pair. For example, it is clear that

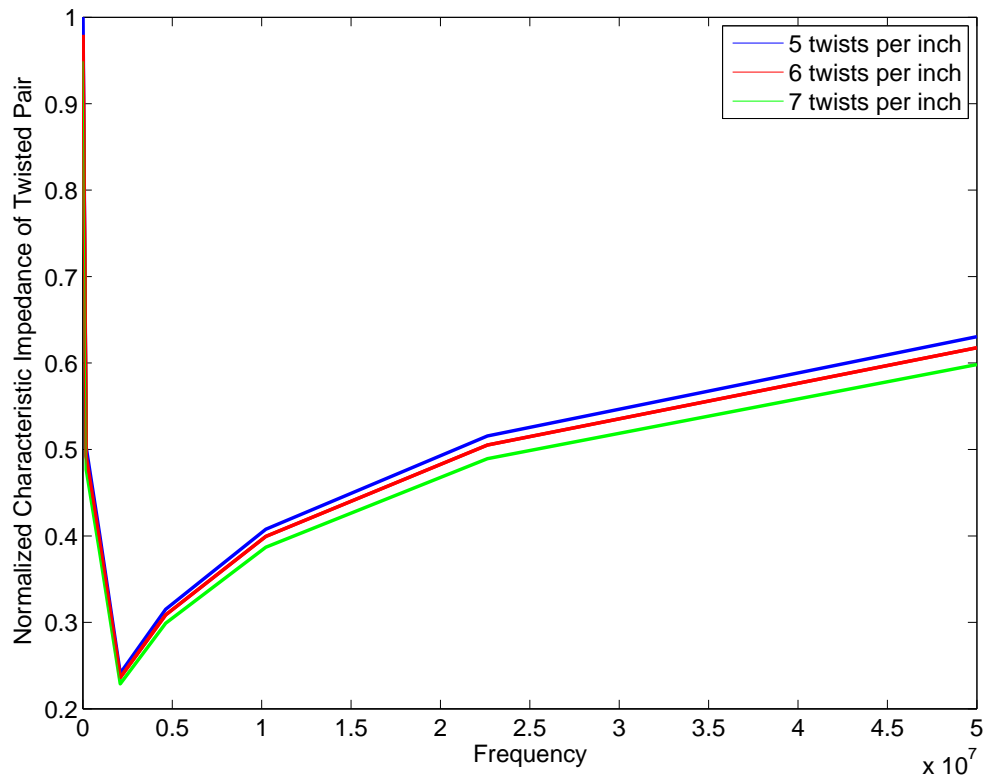


Figure 3.6: Characteristic impedance of a twisted-pair as a function of frequency for twisted pair period of 5, 6, and 7 twists-per-inch.

the twist distribution on the cable is continuous, unimodal (having a single local extrema) and zero at either end (this will be discussed in more detail in the following paragraphs). Furthermore, the matrix Green's functions, while providing us with a transfer coefficient of the voltage and current waves traveling the cable, are not the parameter of concern.

Instead, given a statistical model of how the twist is distributed along the cable, we can use the model to generate different distributions and then use these distributions to calculate the change in voltage induced on the sense elements. How the distributions are used to calculate the change in voltage induced on the sense will be discussed after the model for the distribution is laid out. Comparing these results to measured results, we can determine if our model is reasonable.

As mentioned above, there are a few characteristics of how the twist is distributed that are known by simple observation. The single twist is distributed in a unimodal fashion along the cable; the distribution has a single local maximum along the length. Furthermore, at the sense element and probe electronic ends, the twist is the natural twist of the cable (the distribution density of the twist goes to zero). We also know that the distribution is smooth and continuous with its derivative equal to 0 at the local maximum along the cable.

The characteristics of the distribution that are uncertain are the location of the maximum along the cable and what percentage the single twist is distributed to the left and to the right of the maximum. From observations of multiple twists and untwists of a JENTEK prototype cable, it became clear that the twist distribution maximum, occurring at x' (for the prototype test cable $0 \leq x' \leq 1$ since the cable is 1 meter long), generally occurs in the middle half of the cable. So a reasonable distribution was $x' \sim N(\frac{1}{2}, \frac{1}{32})$. Furthermore the percent of the distribution to the left of x' , p_{left} , seemed to vary within 10% of the length to the left of x' . Therefore, a reasonable distribution was $p_{left} \sim N(x', \frac{1}{160})$. Clearly, $p_{right} = 1 - p_{left}$ for the case

of the single twist. One final condition imposed on the distribution function was that its second derivative was negative at x' . This made the distributions more realistic.

Using a polynomial spline fit of degree four, all of the above conditions were satisfied. Figure 3.7 shows some example distribution densities that are from the model described by Equations (3.7)-(3.10).

$$\text{For } 0 \leq x \leq x', \quad f_1(x) = a_1 + b_1x + c_1x^2 + d_1x^3 + e_1x^4 \quad (3.7)$$

$$\begin{bmatrix} 1 & 0 & 0 & 0 & 0 \\ 0 & 0 & 0 & 0 & 1 \\ 0 & 1 & 2x' & 3x'^2 & 0 \\ 0 & 0 & 2 & 6x' & 0 \\ 0 & \frac{1}{2}x'^2 & \frac{1}{3}x'^3 & \frac{1}{4}x'^4 & 0 \end{bmatrix} \begin{bmatrix} a_1 \\ b_1 \\ c_1 \\ d_1 \\ e_1 \end{bmatrix} = \begin{bmatrix} 0 \\ 0 \\ 0 \\ -1 \\ \rho_{left} \end{bmatrix} \quad (3.8)$$

$$\text{For } x' \leq x \leq 1, \quad f_2(x) = a_2 + b_2x + c_2x^2 + d_2x^3 + e_2x^4 \quad (3.9)$$

$$\begin{bmatrix} 1 & 1 & 1 & 1 & 1 \\ 1 & x' & x'^2 & x'^3 & x'^4 \\ 0 & 1 & 2x' & 3x'^2 & 4x'^3 \\ 0 & 0 & 2 & 6x' & 12x'^2 \\ 1 - x' & \frac{1}{2} - \frac{1}{2}x'^2 & \frac{1}{3} - \frac{1}{3}x'^3 & \frac{1}{4} - \frac{1}{4}x'^4 & \frac{1}{5} - \frac{1}{5}x'^5 \end{bmatrix} \begin{bmatrix} a_1 \\ b_1 \\ c_1 \\ d_1 \\ e_1 \end{bmatrix} = \begin{bmatrix} 0 \\ f_1(x') \\ 0 \\ -1 \\ \rho_{left} \end{bmatrix} \quad (3.10)$$

For each possible distribution of a twist along the JENTEK prototype cable generated by the above model, the new characteristic impedance of the cable can be determined. The model explains how each twist period varies, and MCTLT produces the characteristic impedance transfer function for each twist period. Starting from the probe electronics end of the cable, the first twist period can be seen as its own transmission line with input impedance determined by the termination in the probe electronics unit, Z_L , and its own characteristic impedance, Z_0 , by the following

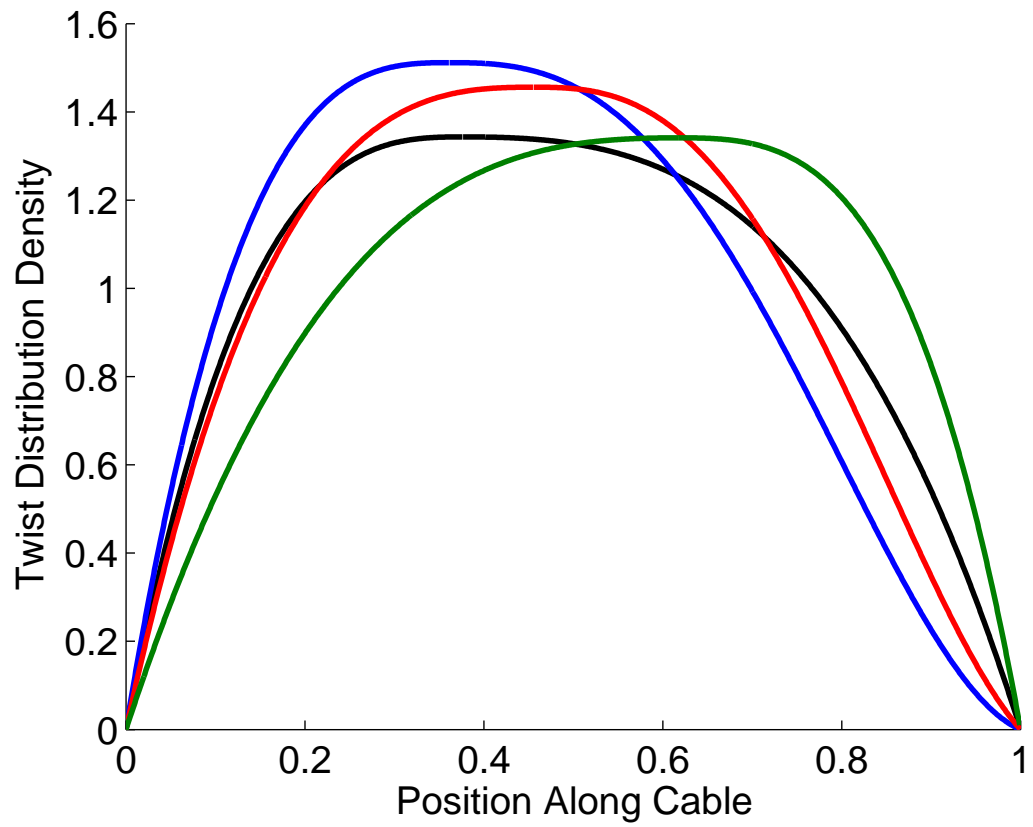


Figure 3.7: Four possible twist distribution densities given the model described by Equations (3.7)-(3.10).

equation:

$$Z_{in} = Z_0 \frac{Z_L + jZ_0 \tan(\beta l)}{Z_0 + jZ_L \tan(\beta l)} \quad (3.11)$$

where β is the wavenumber of the twisted transmission line and l is the length of the period (since the entire transmission line is only one period). This Z_{in} is then used as the load impedance on the next period of the cable and, so on, all the way down the line until the final Z_{in} represents the input impedance of the entire cable. This can be used as the Z_L needed for Equation (3.4). Comparing this result to the untwisted cable we can determine how far the impedance measurement will shift due to the cable twisting across frequencies. Figure 3.8 shows how the impedance measurement is predicted to change across frequencies due to a single loosening twist along the cable. Measurement data is overlaid and clearly shows that the model reflects reality.

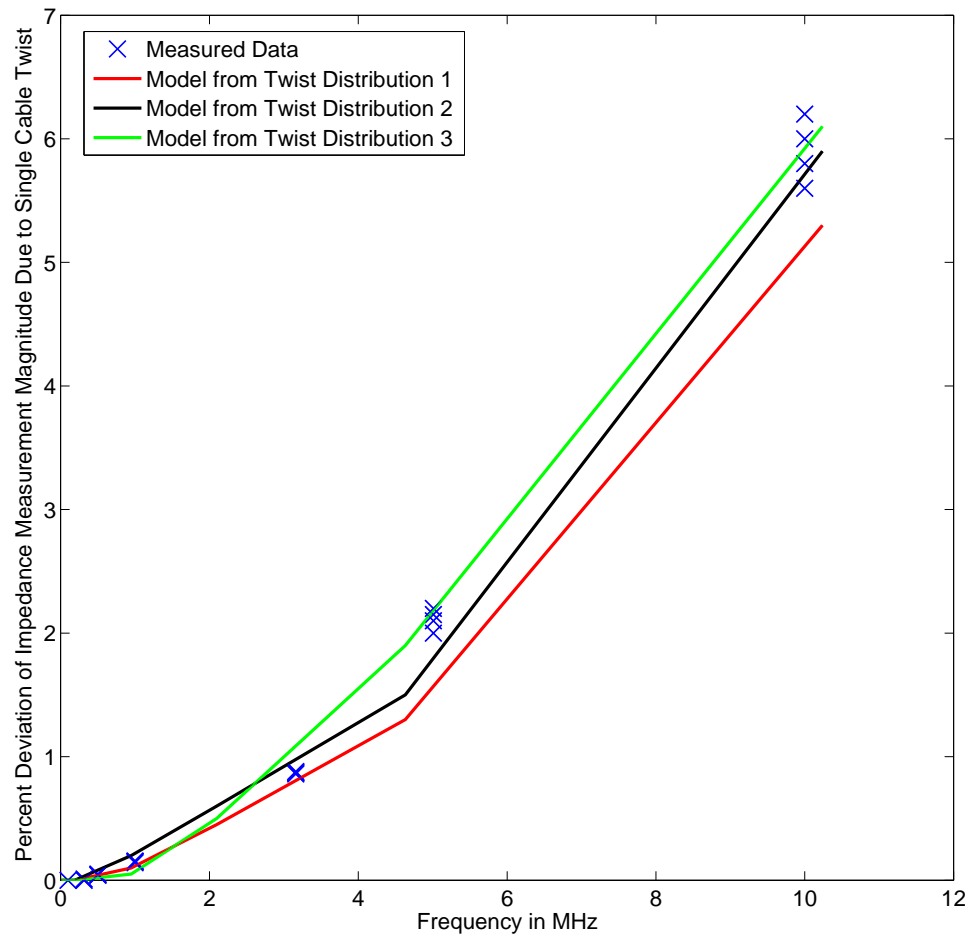


Figure 3.8: Measurement data overlaid on model data for how an impedance measurement is affected by a single loosening twist of the JENTEK prototype cable.

CHAPTER 4

CONCLUSION

The preceding has provided a quantitative investigation of the JENTEK prototype cabling and its sources of noise. Specifically, this thesis provided an analysis of how external electromagnetic radiation and shape changes to the cable could introduce variation in an impedance measurement. In Chapter 2 it was determined that, under most conditions, the shielding around the prototype cabling was sufficient to isolate the drive twisted pair from the sense element twisted pairs, and both of them from ambient electromagnetic radiation. A method for determining the possible interaction between the radiation and the measured signal was presented. Finally, it was shown that in the presence of a high-powered emitter such as a radar, a stronger shield should be considered.

Chapter 3 provided an analysis of how shape changes to the cable could affect an impedance measurement. By loosening or tightening the twist period of the twisted pairs used in the prototype cable, the characteristic impedance of the sense element twisted pair was altered. This caused a shift in the induced voltage on the sense element, corrupting the impedance measurement. A model was presented for how the twist was distributed along the cable that seemed representative. This model was able to predict impedance response to the twisting of the cable across frequency. It was shown that choosing a different twist period, either tighter or looser, would not solve this problem due to the need to maintain a balanced differential line and the physical limitations of the wire.

Future work could involve refining the model to extend the applicable frequency

range as well as developing a model of how bending changes the twist period of a twisted pair. Another line of research would be to investigate methods of providing signal amplification at the sensor in order to eliminate (or minimize) any sensitivity to variations in cable shape.

REFERENCES

- [1] N. J. Goldfine, D. E. Schlicker, A. P. Washabaugh, V. A. Zilberstein, and V. Tsukernik, "Surface mounted and scanning spatially periodic eddy-current sensor arrays," U.S. Patent 6,952,095 B1, October 4, 2005.
- [2] J. R. Melcher, "Apparatus and methods for measuring permeability and conductivity in materials using multiple wavenumber magnetic interrogations," U.S. Patent RE 36,986, December 12, 2000.
- [3] J. R. Melcher, "Apparatus and methods for measuring permeability and conductivity in materials using multiple wavenumber magnetic interrogations," US Patent 5,015,951, May 1991.
- [4] N. J. Goldfine, "Uncalibrated, absolute property estimation and measurement optimization for conducting and magnetic media using imposed ω -k magnetometry," Sc.D. Dissertation, Massachusetts Institute of Technology, Cambridge, MA, September, 1990.
- [5] N. J. Goldfine, "Magnetometers for improved materials characterization in aerospace applications," *Materials Evaluation*, vol. 51, no. 3, pp. 396-405, March 1993.
- [6] N. J. Goldfine, V. Zilberstein, A. Washabaugh, D. Schlicker, I. Shay, and D. Grundy, "Eddy current sensor networks for aircraft fatigue monitoring," *Materials Evaluation*, vol. 61, no. 7, pp. 852-859, July 2003.
- [7] M. A. Lee and K. E. Schmidt, (2001, July), Supplement to Thin Wire Scattering applet, Arizona State University, [Online]. Available: <http://fermi.la.asu.edu/ccli/applets/wire/supp.pdf>.
- [8] C. A. Balanis, *Advanced Engineering Electromagnetics*, New York: John Wiley & Sons, 1989.
- [9] J. H. Van Vleck, F. Bloch, and M. Hammermesh, "Theory of radar reflection from wires or thin metallic strips," *Journal of Applied Physics*, vol. 18, pp. 274, 1947.
- [10] S. Chang and V. V. Liepa, "Measured back scattering cross section of thin wires," University of Michigan Radiation Laboratory report no. 8077-4-T, May 1967.

- [11] F. M. Tesche, "Shielded cable models," report written as EMC consultant, June 11, 2007.
- [12] TechFest, (1999-2002), "IBM cabling system technical summary," [Online]. Available: <http://www.techfest.com/networking/cabling/ibmcs.htm>.
- [13] Gore, (2010), "Gore shielded twisted pair, controlled impedance wire," [Online]. Available: <http://www.gore.com/MungoBlobs/906/996/JK060427-05-Controlled-Impedance.pdf>.
- [14] K. Blattenberger, "Electronic warfare and radar systems engineering handbook - radiation hazards," [Online]. Available: <http://www.rfcafe.com/references/electrical/ew-radar-handbook/radiation-hazards.htm>.
- [15] P. Lefferson, "Twisted magnet wire transmission line," *IEEE Transactions on Parts, Hybrids, and Packaging*, vol. 7, no. 4, pp. 148-154, Dec. 1971.
- [16] S. Legale, (2000), "Inductance calculations: Square loop," [Online]. Available: http://www.technick.net/public/code/cp_dpage.php?aiocp_dp=util_inductance_square.
- [17] G. J. Kissel, "Localization and the invariant probability measure for a structural dynamic system," *Proc. SPIE*, vol. 7286, 2009.

AUTHOR'S BIOGRAPHY

Scott Andrew Denenberg was born on April 7, 1985, in Trumbull, Connecticut. He graduated with honors from Harvard University with an S.B. in Electrical Engineering and Computer Science in 2007. As part of his senior project, Scott studied and mathematically modeled propagation and damping of solitons through non-linear transmission lines. This work culminated in the co-authored paper, "Ordered and chaotic electrical solitons: communication perspectives," *IEEE Communications Magazine*, Dec. 2006, pp. 126-135.

Scott began working at JENTEK Sensors immediately after graduation. His work has resulted in three co-authored papers and two co-authored patent applications:

1. "Magnetic stress gages for monitoring bridges," ASNT NDE/NDT for Highways and Bridges: Structural Materials Technology (SMT) 2008, Oakland, CA, September 8-12, 2008.
2. "Magnetic stress gages for torque and load monitoring in rotorcraft," American Helicopter Society (AHS) 64th Annual Forum, Montreal, Canada; April 29-May 1, 2008.
3. "Multi-directional magnetic stress gages," 54th International Instrumentation Symposium; Propulsion Instrumentation Working Group (PIWG), Pensacola, FL, May 5-8, 2008.
4. "Magnetic stress gages for torque and load monitoring," U.S. Patent provisional filing date March 25, 2008.
5. "Magnetic stress gages for torque and load monitoring in rotorcraft," U.S. Patent

provisional filing date April 29, 2008.

Scott is continuing his graduate education at the University of Illinois at Urbana-Champaign (UIUC) under the guidance of Professor Andreas Cangellaris. Scott plans to pursue his doctorate at UIUC while continuing his work and research for JENTEK Sensors.